Interleukin-17A Mediates Cardiorenal Injury In Oxalate Nephropathy

- 3 Moritz I. Wimmer^{1,2,3,4}, Martin Reichel^{4,5}, Arne Thiele^{1,2,3,4}, Alex Yarritu, ^{1,2,3,4}, Ariana Matz-Rauch^{1,2,3,4},
- 4 Harithaa Anandakumar^{1,2,3,4}, Luisa Hernandez Götz¹, Till Robin Lesker⁶, Olena Potapenko^{1,2,3,4},
- 5 Natnael Gebremedhin^{1,2,3,4}, Wibke Anders^{1,2,3,4}, Sarah V. Liévano Contreras^{2,3,5}, Rongling Wang^{2,3,5},
- 6 Olivia Nonn^{1,2,3}, Gabriele G. Schiattarella^{1,2,3,5,7,8}, Franz Schaefer⁹, Johannes Holle^{1,2,3,10}, Till Strowig^{6,11},
- Alma Zernecke¹², Kai-Uwe Eckardt⁴, Felix Knauf^{4,5,13}, Nicola Wilck^{1,2,3,4,*}, Hendrik Bartolomaeus^{2,3,12,*,†}
- 9 ¹Experimental and Clinical Research Center (ECRC), a cooperation of Charité Universitätsmedizin
- 10 Berlin and Max Delbrück Center for Molecular Medicine, Berlin, Germany.
- ²Max-Delbrück-Center for Molecular Medicine in the Helmholtz Association, Berlin, Germany
- 12 ³DZHK (German Centre for Cardiovascular Research), partner site Berlin, Germany.
- 13 ⁴Department of Nephrology and Medical Intensive Care, Charité Universitätsmedizin Berlin,
- 14 corporate member of Freie Universität Berlin and Humboldt-Universität zu Berlin, Berlin, Germany.
- 15 Max Rubner Center for Cardiovascular Metabolic Renal Research, Charité Universitätsmedizin
- 16 Berlin, Berlin, Germany.
- 17 ⁶Department of Microbial Immune Regulation, Helmholtz Center for Infection Research,
- 18 Braunschweig, Germany
- 19 ⁷Friede Springer Cardiovascular Prevention Center at Charité Universitätsmedizin Berlin, Berlin,
- 20 Germany

1

2

8

- ⁸Division of Cardiology, Department of Advanced Biomedical Sciences, Federico II University, Naples,
- 22 Italy.
- ⁹Division of Pediatric Nephrology, University Children's Hospital, Heidelberg, Germany
- 24 ¹⁰Department of General Pediatrics and Hematology/Oncology, University Children's Hospital,
- 25 University Hospital Tübingen, Tübingen, Germany
- ¹¹Center for Individualized Infection Medicine (CiiM), a joint venture between the Helmholtz-Center
- for Infection Research (HZI) and the Hannover Medical School (MHH), Hannover, Germany

- 28 ¹²Institute of Experimental Biomedicine, University Hospital Würzburg, Würzburg, Germany
- 29 ¹³Division of Nephrology and Hypertension, Mayo Clinic, Rochester, Minnesota, USA.
- 30 *equal contribution

31 †Correspondence: bartolomae_h@ukw.de

34

35

36

37

38

39

40

41

42

43

44

45

46

47

48

49

50

51

52

53

54

Abstract Aims: Cardiovascular disease (CVD) is the leading cause of mortality in chronic kidney disease (CKD). While CKD is known to give rise to systemic inflammation, its inciting factors remain poorly defined. Oxalate, long implicated in rare genetic kidney disorders, accumulates with decreased kidney function and has emerged as a driver of inflammation and independent risk factor for CVD. Here, we investigate the immunological mechanisms linking oxalate nephropathy to systemic inflammation, cardiac damage and kidney injury. Methods and Results: Oxalate nephropathy was induced in C57Bl6/N mice via an oxalate-enriched diet. Oxalate induced systemic immune activation, renal fibrosis, and cardiac remodeling, including pulmonary congestion with systolic and diastolic dysfunction. Flow cytometry analysis identified interleukin (IL)-17A as a dominant inflammatory effector, with expansion of Th17 and Th17-like Treg in the kidney, intestine, and spleen. Bulk mRNA sequencing confirmed these findings. Confirming the oxalate-IL-17A relationship, plasma IL-17A was elevated in patients with primary hyperoxaluria. Gut microbiome analysis by 16S amplicon sequencing showed only mild oxalate-induced alterations in mice. However, soluble oxalate directly enhanced Th17 polarization and disrupted mitochondrial respiration in vitro. In vivo, antibody-mediated (clone: 17F3) IL-17A blockade decreased cardiac fibrosis, reduced neutrophil infiltration, and partially restored cardiac function in oxalate-fed mice. Conclusions: Our study identifies oxalate as a systemic immunometabolic stressor and IL-17A as a central mediator of oxalate-induced cardiorenal injury. These findings establish the oxalate-IL-17A axis as a mechanistic link between CKD and CVD and suggest IL-17A inhibition as a potential therapeutic strategy to reduce cardiovascular damage in CKD.

Translational Perspective

This study advances our understanding of targetable mediators of the cardiovascular risk in chronic kidney disease (CKD). We identify the organic anion oxalate, beyond its traditional role in crystal-induced kidney damage, as a systemic immunometabolic stressor. We demonstrate that oxalate induces IL-17A—mediated inflammation and thereby contributes to maladaptive cardiac remodeling. Therapeutic blockade of IL-17A protects against oxalate-induced cardiorenal injury, highlighting the oxalate—IL-17A axis as a relevant and druggable link between CKD and cardiovascular disease.

1. Introduction

62

63

64

65

66

67

68

69

70

71

72

73

74

75

76

77

78

79

80

81

82

83

84

85

86

87

88

The recognition of oxalate as a relevant disease driver of chronic kidney disease (CKD) has recently expanded beyond its traditional association with rare disorders, such as primary and enteric hyperoxaluria^{1, 2}. Oxalate-induced nephropathy is characterized by the deposition of calcium oxalate crystals, frequently accompanied by tubular injury, interstitial nephritis, and progressive fibrosis³. Surprisingly, kidney biopsy cohorts have demonstrated that tubular oxalate crystal deposition is observed across a broad spectrum of kidney diseases¹, indicating that oxalate crystal deposition is not confined to rare genetic disorders but occurs more frequently in kidney disease⁴. In fact, oxalate crystals in kidney biopsies are now considered a marker of poor prognosis, with increased risk of progression to kidney failure^{1, 5}. In addition, recent evidence suggests that high soluble plasma oxalate is a risk factor for adverse outcomes beyond kidney diseases, including cardiovascular morbidity and mortality^{4, 6}. Analyses of the German Diabetes Dialysis (4D) Study cohort demonstrated that elevated serum oxalate in hemodialysis patients independently correlates with a 40% increased risk of cardiovascular events and a 62% higher risk of sudden cardiac death⁶. These findings, validated in a separate cohort, suggested elevated serum oxalate as a novel contributor to cardiovascular disease (CVD) in CKD6. In line, serum oxalate was associated with CVD in a cohort of Japanese dialysis patients⁷. Interestingly, cardiovascular abnormalities have long been described in experimental oxalate nephropathy8. Experimental work highlighted the central role of the innate immune system, particularly the NLRP3 inflammasome, in mediating oxalate-induced renal injury^{9, 10}. Activation of the NLRP3 inflammasome by calcium oxalate crystals triggers caspase-1 activation and subsequent IL-1ß release, thereby promoting a robust inflammatory response and renal damage⁹. This process is further amplified by the generation of reactive oxygen species (ROS) and mitochondrial dysfunction, which together sustain a pro-inflammatory microenvironment and drive the progression of nephropathy¹¹. Recent studies have demonstrated altered gut microbiota composition in CKD12 and oxalate nephropathy specifically13. Since specific bacteria metabolize oxalate, probiotic approaches have been tested in primary hyperoxaluria (PH)¹⁴.

Collectively, clinical and experimental evidence emphasize the role of oxalate in promoting kidney and cardiac injury, with sterile inflammation, inflammasome activation and downstream cytokine networks serving as central effectors of disease progression. The current study aims to broaden the mechanistic understanding of oxalate-induced inflammation including the microbiome and the enteric immune cell niche, and identifies IL-17A as an essential cytokine effector driving cardiorenal damage.

2. Methods

94

95

96

97

98

99

100

101

102

103

104

105

106

107

108

109

110

111

112

113

114

115

116

117

118

119

Please see the supplemental methods for full experimental procedures.

2.1. Data availability

The authors declare that all supporting data and analytical methods are available within the article and its data supplement. The data, analytical methods, and study materials that support the findings of this study are available from the corresponding author.

2.2. Animal studies

All animal experiments were performed in accordance with the German/ European law for animal protection. Animal protocols were approved by the responsible authorities in Berlin, Germany (LaGeSo, G0079/18 and G0047/23). All animal experiments were performed at the Max Rubner Center for Cardiovascular Metabolic Renal Research, Charité - Universitätsmedizin. Male 8- to 12-wk-old C57Bl/6N mice were obtained from Charles River Laboratories and housed at a 12-hour day:night cycle with free access to water and food pellets. To maintain constant calcium levels in the drinking water, we used water from sterile hydropac pouches (Plexx B.V.). Mice were kept in isolated ventilated cages under specific pathogen-free conditions. Prior to experimental diets, animals were kept on a standard chow diet (Chow, ssniff Spezialdiäten GmbH, V1534-300). Synthetic mouse diets with varying sodium oxalate concentrations of either high oxalate (Ox, 0.67% sodium oxalate, S7042-E010), or control (Ctrl, 0% oxalate, \$7042-E005) were obtained from ssniff Spezialdiäten GmbH. Oxalate-containing diets were virtually calcium free to provide oxalate in soluble form. Exact composition of the purified diets is provided in Table S1. Animals were placed on the Ox diet for of up to 14 days after being placed on Ctrl for 3 days. After 14 days or when approaching 20% relative body weight loss animals were sacrificed by bleeding via the retroorbital venous plexus in isoflurane narcosis (5% isoflurane-air mixture) with subsequent cervical dislocation. Collected blood was anticoagulated with 0.5M EDTA (Merck).

Animal randomization was performed in a weight-stratified, cage-wise manner. Mice were excluded upon reaching 20% relative weight loss in compliance with the 3R principles (Replacement, Reduction, Refinement). Blinding was not performed during the in vivo experiment, as weight loss, food color, and i.p. injections indicated treatment group. However, blinding was performed for all subsequent analyses. For the inflammation and microbiome trial, groups of two mice were housed per cage. After the sacrifice of the control animal (n=7), the paired experimental animal (n=7) underwent the study protocol. The study was primarily designed to explore inflammatory and microbiome-related changes and therefore no formal a priori sample size calculation was performed. Single-housing was implemented after control sacrifice to avoid cage effects in microbiome analyses. For the cardiovascular investigation experiments, animals were housed in groups of four per cage. Control animals (n=12) were fed the Ctrl diet, and experimental animals (n=12) received the Ox diet. The primary outcome parameters for sample size calculation were cardiovascular damage endpoints, determined based on effect sizes reported by Mulay and colleagues8. In the IL-17A blockade trial, groups of two mice per cage were all fed the Ox diet. Mice received intraperitoneal injections thrice weekly of either 250 µg anti-IL-17A antibody (clone: 17F3; BioXCell, n=12) or isotype control antibody (clone: MOPC-21; BioXCell, n=12) in 200 μl isotonic saline (Braun). All mice underwent a two-week handling training period before trial start to reduce stress during injections. The primary outcome parameters for sample size calculation were blood urea nitrogen (BUN) levels and lung wet/dry weight ratios, based on differences observed in the cardiovascular trial. For in vitro studies, immune cells were isolated from C57BI/6 wild-type mice from in-house breeding at the Max Delbruck Center for Molecular Medicine. Animals were kept on a constant 12-hour day:night cycle and had ad libitum access to standard chow diet and drinking water (tap water). Mice were sacrificed using isoflurane.

2.3. Flow cytometry

120

121

122

123

124

125

126

127

128

129

130

131

132

133

134

135

136

137

138

139

140

141

142

143

144

145

146

For flow cytometry analysis, dead cells were labeled with a Live/Dead Fixable Aqua Dead Cell Stain Kit at 405 nm excitation (Thermo Fisher), followed by surface antibody staining (Table S2 for baseline trial, Table S3 for IL-17 blockade trial) in PBS + 0.5% BSA + 2 mM EDTA together with Fc blocking reagent (Miltenyi Biotec). Cells were first permeabilized for intracellular staining and then stained with intracellular antibodies (Table S2 and S3) using the eBioscience FoxP3/ Transcription Factor Staining Buffer Kit (Thermo Fisher). All steps were performed for 30 min at 4°C. Cells were recorded on a BD LSRFortessa Cell Analyzer (BD Bioscience) using BD FACS Diva software (BD Bioscience) and analyzed using FlowJo 10.8.1 (BD Bioscience). In the baseline trial, we quantified approximately 80 immune cell subsets. For the non-T cell gating we employed instead of classical hierarchical gating a logical based AND/OR boolean gating strategy. The details of the immune cell population definitions are presented in the supplementary table (Table S4) and the respective gating strategy (Supplementary Figure S1). In the IL-17 blockade trial we performed a more targeted quantification of immune cell subsets. The details of the immune cell population definitions are presented in the supplementary table (Table S5) and the respective gating strategy (Supplementary Figure S1).

2.4. RNA preparation and gene expression analysis

Total RNA was isolated from kidneys using Trizol following the manufacturer's protocol. From isolated RNA, cDNA was prepared using the High-Capacity cDNA Reverse Transcription Kit (Applied Biosystems). Real-time quantitative PCR was performed using Blue S'Green qPCR Kit (Biozym) on a CFX Opus 384 (Biorad). All gene expression values were normalized using 18S RNA as a housekeeping gene. All primers used for amplification were from Eurofins and are listed in Table S6.

Bulk mRNA sequencing and bioinformatic analysis was performed from 3 mice per group by Novogene (Cambridge, UK). Total kidney RNA was subjected to poly(A) selection to enrich for mRNA. Strand-specific RNA-seq libraries RNA-seq libraries were prepared using standard Illumina protocols. Sequencing was performed on an Illumina NovaSeq 6000 platform via 150 bp paired-end sequencing (PE150). Each sample was sequenced to a depth of approximately 12 G of raw data. Fastq files were quality-filtered and adapter-trimmed using fastp, followed by alignment to the reference genome with

HISAT2 (2.2.1). Gene-level counts were generated using featureCounts (2.0.6), and differential expression analysis was performed with DESeq2 (1.42.0). Gene ontology (GO) enrichment analyses were performed on differentially expressed genes with the following cut-off, an according to Benjamini-Hochberg false discovery rate q value of < 0.001 and log2FC > 1.5 or < 1.5 using gProfiler2 (v0.2.3)¹⁵. Cardiac RNA was isolated from cardiac tissue of the heart tip using the Qiagen RNEasy Kit, micro according to manufacturer's protocol. cDNA was synthesized using the High-Capacity cDNA Reverse Transcription Kit (Applied Biosystems). Real-time quantitative PCR was performed using the TaqMan Multiplex Master Mix (Applied Biosystems) on a QuantStudio 5 (Thermo Fisher). All primers used for amplification were obtained from IDT and probes from Thermo Fisher and are listed in Table S6.

2.5. Statistical Analyses

For Chow vs. Ox and Ctrl vs. Ox comparisons, unpaired, two-tailed Mann-Whitney U-test was used for determining statistical significance. Since we followed a pre-specified hypothesis in the IL-17A blockade trial, unpaired, one-tailed Mann-Whitney U-test was used for determining statistical significance. All PCA shown were computed using Euclidean distance. For microbiome analysis, univariate testing was performed using two-tailed Wilcoxon signed rank test. Effect sizes were calculated using Cliff's delta. Microbiome PCoA is based on Bray–Curtis dissimilarity. For multiple testing, false discovery rate correction (FDR) according to Benjamini-Hochberg was performed. Unless otherwise stated, analysis was performed in R (v4.4.3) with the following packages: readr, readxl, broom, tidyverse, phyloseq, vegan, ggpubr, orddom, EnhancedVolcano, tidyHeatmap, and ComplexHeatmap packages and visualized using ggplot2. Th17 differentiation assays and seahorse experiments were analyzed in GraphPad Prism (GraphPad Prism v10.1.1) by Student's T-test.

P-values below 0.05 were considered significant.

3. Results

198

199

200

201

202

203

204

205

206

207

208

209

210

211

212

213

214

215

216

217

218

219

220

221

222

223

3.1. Systemic and renal pathophysiological alterations in oxalate-fed mice

To model oxalate nephropathy, mice were fed a purified oxalate-enriched diet (Ox) for up to 14 days using an established protocol (Fig. 1a)8. In accordance with ethical guidelines, experiments were terminated when mice neared a 20% loss in body weight. Ox feeding led to significant kidney injury by day 10, accompanied by systemic wasting as observed in both absolute and relative weight loss (Fig. 1b, S2a). Plasma retention parameters confirmed damage to the kidneys (Fig. 1c). These changes were paralleled by a marked increase in kidney mass, suggestive of inflammation (Fig. S2b). Elevated plasma and urinary oxalate levels confirmed effective dietary oxalate loading and impaired oxalate clearance (Fig. 1d, S2c). Renal gene expression of damage-associated genes, including Lcn2 and Havcr1, was elevated in Ox mice (Fig. 1e, S2d), along with a previously described strong induction of inflammasome-related genes such as II1b (Fig. S2e-f). Bulk mRNA sequencing of kidney tissue further revealed increased expression of pro-inflammatory mediators (II1b, Tnf, Cd44) and fibrosis-associated genes (Fn1), indicative of parenchymal damage and inflammatory activation (Fig. 1f, S2g). Pathway enrichment analysis revealed broad transcriptional reprogramming, with enrichment for pathways associated with immune cell trafficking (e.g. T cell extravasation) and cytokine signaling (e.g. macrophage cytokine production) pathways (Fig. 1g). To delineate immune dynamics, flow cytometry was performed on leukocytes isolated from the spleen, kidney, small intestinal lamina propria (siLPL), and colonic lamina propria (cLPL). A heatmap of kidney immune populations demonstrated distinct compositional shifts in Ox mice (Fig. 1h), while principal component analysis (PCA) of organ-specific immune profiles highlighted both tissue-specific signatures and oxalate nephropathy-driven clustering (Fig. 1i). Absolute quantification confirmed a systemic expansion of leukocyte populations across all examined tissues (Fig. 1j-k, S2h-i). In line with previous reports ¹⁶, Ox mice exhibited a robust increase in total macrophage abundance (Fig. S2j), with a strong expansion of pro-inflammatory subsets (Fig. S2k-m).

These findings collectively underscore a diet-induced, multiorgan response characterized by renal inflammation, fibrotic priming, and systemic immune activation.

3.2. Microbiome response to dietary oxalate

Gut microbiome alterations have been recently implicated in the pathogenesis of experimental oxalate nephropathy¹³. Therefore, fecal microbiome analysis was performed using 16S rRNA gene sequencing. Mice were initially maintained on a standard chow diet (Chow), then switched to a purified control diet (Ctrl), followed by the addition of oxalate to the purified diet (Ox). To control for coprophagia and cage effects, mice were single-housed. While alpha diversity indices (Fig. S3a, b) decreased upon transition from chow to purified control diet, subsequent exposure to Ox showed no effect on alpha diversity. Similarly, beta-diversity was most affected by the purified diet (Fig. S3c). However, focusing on samples collected during the purified diet phase with and without Ox, we observed specific clustering by timepoint (Fig. S3d). At the phylum level, overall microbiome composition remained stable across the intervention (Fig. S3e). Differential abundance analysis at the genus level on day 5 and day 10 of Ox showed an increase among others in *Lactobacillus* and a decrease in *Parasutterella* and *Prevotella* (Fig. S3f-h). Overall, changes in microbiome composition and diversity were relatively modest compared to the pronounced immune alterations observed in this study. It is important to note that genus-level changes observed in Ox were only identified in exploratory analyses and were not significant after FDR correction (Supplementary Data 1).

3.3. Systemic Interleukin-17A and shared Th17/Treg17 signatures across renal and intestinal

compartments

To examine conserved patterns of immune response across different organs, we performed unsupervised clustering of flow cytometry data by PCA showing a clear segregation of Ox and Chow samples (Fig. 2a). We focused on the top 15 immune cell populations best separating Ox from Chow in the PCA of each organ (Fig. 2b) and identified conventional T helper cells (Tconv) expressing RORyt⁺ (Th17) and regulatory T cells (Treg) expressing (Treg17) as overlapping core subsets increased in all

252

253

254

255

256

257

258

259

260

261

262

263

264

265

266

267

268

269

270

271

272

273

274

275

276

277

three organs (Fig. 2c-e). These populations exhibited pronounced expansion in Ox mice (Fig. 2d, e). RORyt is the lineage transcription factor for IL-17A-producing cells. We confirmed increased IL-17A production by Tconv across organs, while only Treg in the kidney produced large amounts of IL-17A in Ox mice (Fig. S4a-f). Analysis of these immune subsets in the spleen, as a representative systemic lymphoid organ, confirmed an increase in Th17 (Fig. 2f) and a non-significant increase in Treg17 (Fig. 2g). To test whether the IL-17A⁺/ RORγt⁺ phenotype was exclusive to Tconv and Treg, we investigated multiple lymphocyte subpopulations. Interestingly, we found increased frequencies of various IL-17A producing/ RORyt expressing immune cell subsets in the kidney, among others innate lymphoid cells type 3 (ILC3, Fig. S4g, h), $\gamma\delta$ T cells ($\gamma\delta$ 17, Fig. S4i, j), and cytotoxic T cells (Tc17, Fig. S4k, l). For Tc17, only the increase in RORyt expression reached statistical significance (Fig. S4k) while IL-17A production showed a non-significant increase (Fig. S4I). In line, bulk mRNA sequencing of kidney tissue from Ox mice showed a robust enrichment of pathways governing IL-17A production, signal transduction, and Th17 lineage commitment (Fig. 2h). A heatmap of genes from the IL-17A signaling pathway revealed a marked increase in expression in the highoxalate group, indicating strong activation of this inflammatory axis (Fig. 2i). To test whether IL-17A is similarly upregulated in patients with markedly elevated serum oxalate, we analyzed plasma IL-17A levels of eight patients with primary hyperoxaluria (PH) from the 4C Study¹⁷. Compared to 20 healthy individuals, PH patients showed significantly elevated IL17A serum levels (Fig. 2i). Taken together, the concurrent upregulation of IL-17A transcriptional networks and expansion of Th17/Treg17 populations across kidney and intestinal compartments highlights oxalate as a driver of systemic immune activation.

3.4. Cardiac remodeling and cardiovascular inflammation in oxalate-diet-fed mice

Since chronic inflammation generally and IL-17A specifically play a major role in cardiovascular remodeling¹⁸, we next investigated Ox-induced cardiac remodeling. To account for potential effects of the purified diet, mice on purified diet (Ctrl) were included for comparison (Fig. 3a). Mice subjected to

279

280

281

282

283

284

285

286

287

288

289

290

291

292

293

294

295

296

297

298

299

300

301

302

303

304

Ox recapitulated the renal wasting phenotype observed in the prior experiment, characterized by reduced body weight and elevated blood urea nitrogen (BUN) (Fig. 3b-c). Cardiac involvement was evidenced by a decreased heart weight-to-tibia length ratio, indicating cardiac atrophy (Fig. 3d), and an increased lung wet-to-dry weight ratio, consistent with pulmonary congestion secondary to impaired cardiac function (Fig. 3e). Echocardiographic evaluation revealed combined systolic and diastolic dysfunction, evidenced by a reduced left ventricular ejection fraction alongside elevated mitral inflow E/e' and E/A ratios, indicative of increased filling pressures and impaired relaxation (Fig. 3j-k, S5a-b, Table S7). As a histological correlate, we observed increased cardiac fibrosis (Fig. 3f, g) and heightened leukocyte infiltration (Fig. 3f, h) of the myocardium of Ox mice, supporting the presence of myocardial inflammation and pathological structural remodeling (Fig. S5c). Analysis of myocardial mRNA levels revealed an increased Myh7/Myh6 ratio, consistent with a fetal-like transcriptional shift typically associated with adverse ventricular remodeling (Fig. 3f). Concurrent upregulation of cardiac IIIb, S100a8, and S100a9 expression confirmed inflammatory activation of cardiac tissue (Fig. 3g-i). PCA of all clinical cardiovascular parameters, cardiac mRNA expression profiles, and echocardiographic metrics revealed clear segregation of Ox and Ctrl mice (Fig. S5e), highlighting a disease signature driven by oxalate toxicity, extending beyond renal injury to encompass cardiopulmonary derangements.

3.5. In vitro modulation of T cell differentiation and metabolism by oxalate

As inflammation was the most prominent feature observed in Ox mice, we tested whether soluble oxalate directly exhibits pro-inflammatory effects. Since IL-17A production of T helper cells was the major oxalate target *in vivo*, we performed *in vitro* Th17 differentiation experiments. Naïve CD4+ T cells differentiated in the presence of soluble oxalate produced significantly more IL-17A (Fig. 4a). This effect was dose-dependent and occurred stably at doses of 100µM (Fig. 4b). Of note, 100 µmol/L was within the range observed in plasma samples from Ox mice (Fig. 1b).

Next, we investigated potential mediators of the oxalate effects on Th17 polarization. Cellular metabolism and immune cell polarization are closely connected¹⁹. Previously, tubular oxalate toxicity *in vitro* was linked to impaired mitochondrial function²⁰⁻²². Similar effects have been described in

macrophages^{23, 24}. Therefore, we assessed mitochondrial function during Th17 differentiation in the presence and absence of sodium oxalate using real-time extracellular flux analysis. We observed a disturbed mitochondrial function in a mitochondrial stress test in the presence of sodium oxalate (Fig. 4c). ATP-linked respiration was significantly reduced in oxalate-treated cells, indicating a reduced mitochondrial respiration without additional stress tests (Fig. 4e), this was mirrored in a non-significant reduction of basal respiration (Fig. 4d). Additionally, the maximal possible as well as spare respiratory capacity showed non-significant reductions (Fig. 4f, g), indicating a reduced potential of mitochondria to produce energy.

Our experiments thus link increased soluble oxalate with the differentiation of pathological Th17, where oxalate-mediated metabolic shift may create a permissive microenvironment for proinflammatory T cell differentiation.

3.6. In vivo Interleukin-17A blockade ameliorates systemic oxalate-induced pathology

Lastly, we aimed to understand whether IL-17A signaling contributes to the cardiorenal pathology in Ox mice. Therefore, we applied an *in vivo* antibody-based cytokine blockade using an IL-17A-neutralizing antibody i.p. thrice weekly (Fig. S6a, 5a). Compared to control mice (IgG1 control antibody i.p.), IL-17A blockade attenuated systemic wasting, as evidenced by increased body weight (Fig. 5a, b). IL-17A blockade also reduced BUN in Ox mice, indicating attenuated kidney injury (Fig. 5c). In line, histological analysis showed reduced fibrotic remodeling of the kidney (Fig. 5d, e). Transcriptional profiling confirmed this phenotype and showed a downregulation of kidney injury-associated biomarkers, like *Lcn2* (Fig. 5f), and pro-inflammatory cytokines, like *Il1b* and *Tnf* (Fig. 5g, h). Flow cytometry of leukocytes isolated from the kidney and spleen revealed organ-specific immune modulation. Overall, renal leukocyte infiltration decreased with IL-17A blockade (Fig. 5i). In line with previous reports on the close link between IL-17A and neutrophils²⁵, IL-17A blockade led to decreased splenic neutrophils and reduced recruitment of neutrophils into the kidney (Fig. 5j, k). Furthermore, the systemic monocyte subsets in the spleen shifted towards anti-inflammatory Ly6C monocytes (Fig. S6b)²⁶. Treg frequencies in the kidney were reduced under IL-17A blockade (Fig. S6c), while splenic

Treg frequencies remained unchanged (Fig. S5d); a phenotype associated with the resolution of cardiovascular inflammation, as previously shown²⁷. Of note, the frequency of RORyt⁺ T helper cell subsets was unchanged (Fig. S6e-h). IL-17A blockade partially reversed cardiac pathology, with normalized heart weights and reduced pulmonary congestion (Fig. 5I, m). Echocardiography analyses revealed no statistically significant changes, yet an improvement in systolic function was observed (Fig. S6i). Cardiac histology showed an ameliorated phenotype with less interstitial fibrosis and a reduction of infiltrating leukocytes (Fig. 5n-p). In line, myocardial *Mhy7/Mhy6* ratio decreased, confirming attenuated ventricular remodeling (Fig. 5q). Matching, inflammation- and inflammasome-associated mediators (*S100a8*, *S100a9*) were suppressed (Fig. 5r, S6j).

Our findings demonstrate that IL-17A signaling critically mediates multi-organ oxalate toxicity, with blockade of this signaling ameliorating renal and cardiac injury while partially resolving immune dysregulation.

4. Discussion

344

345

346

347

348

349

350

351

352

353

354

355

356

357

358

359

360

361

362

363

364

365

366

367

368

369

370

Our findings establish IL-17A as an important mediator of oxalate-induced systemic inflammation and cardiorenal injury, thereby extending its pathological relevance beyond the kidney. Crystal nephropathies have so far been primarily associated with innate immune cell responses²⁸. The pronounced enrichment of IL-17A-associated transcriptional pathways and systemic expansion of IL-17A-producing T helper cells (Th17/Treg17) across multiple tissues highlight IL-17A in bridging innate and adaptive immunity. IL-17A amplifies inflammation by recruiting neutrophils²⁹ and proinflammatory monocytes³⁰, thereby activating parenchymal cells to produce pro-fibrotic mediators³¹. In line, IL-17A blockade reduces the number of neutrophils and increases the percentage of Ly6C monocytes. Yet, although IL-17A blockade attenuates cardiac and renal damage and body weight loss, the persistence of other inflammatory cues must be considered to maintain a residual degree of pathology³². Oxalate is a known activator of the NLRP3 inflammasome and activates antigen-presenting cells and the production of IL-1 β^{10} , a major driver of Th17 differentiation and IL-17A production³³. IL-17A stimulates epithelial, stromal, and myeloid cells to release chemotactic proteins that recruit neutrophils and monocyte/macrophages²⁹. In line with the neutrophil recruitment observed in our study, IL-17A signaling has been shown to upregulate the neutrophil chemoattractants CXCL1 and CXCL2³⁴. Furthermore, GM-CSF production by Th17 induces the production and mobilization of neutrophils³⁵. For monocytes and macrophages, similar IL-17A effects have been described to be dependent on CCL2 and CCL7³⁶. These findings are supported by our *in vivo* data, which show that IL-17A blockade reduces the recruitment of neutrophils and monocytes/macrophages. This is reflected by the suppressed expression of inflammasome-associated genes³⁷ such as \$100a8 and \$100a9 in the heart. Despite attenuating renal and cardiac inflammation and improving cardiac fibrosis, IL-17A blockade failed to resolve diastolic dysfunction and to completely antagonize the body weight wasting phenotype. This partial efficacy underscores the multifactorial nature of oxalate-induced pathology³⁸, which likely extends beyond IL-17A signaling alone. IL-17A likely functions within a complex inflammatory network, acting synergistically with cytokines such as TNF and inflammasome-derived

372

373

374

375

376

377

378

379

380

381

382

383

384

385

386

387

388

389

390

391

392

393

394

395

396

397

IL-1β to drive tissue injury^{10, 29}. These observations position IL-17A within the complex interplay of innate and adaptive mechanisms, supporting the notion that targeting the broader IL-17A family members or their upstream regulators may be necessary to achieve full therapeutic efficacy. The expansion of RORyt+ IL-17A-producing regulatory T cells (Treg17) in oxalate-fed mice raises questions about their functional properties. Treg17, characterized by the co-expression of transcription factors Foxp3 and RORyt, have been described in mucosal tissues and chronic inflammation, where they retain their suppressive capacity³⁹. However, under inflammatory conditions, Treg17 may adopt a pro-inflammatory phenotype, marked by IL-17A secretion and reduced suppressive efficacy^{40, 41}. Since the net effect of oxalate nephropathy is clearly pro-inflammatory, as evidenced by an ameliorated phenotype following IL-17A blockade, IL-17A production by Treg, especially in the kidney, likely contributes to disease progression. In addition to Th17 and Treg17, our findings highlight IL-17A production by a broader array of immune cells, including $v\delta$ 17 and ILC3s. Of note, $v\delta 17$ were previously implicated in the pathogenesis of oxalate nephropathy⁴². These data support the concept that in chronic sterile inflammation, regulatory lineage markers alone do not predict function, and that IL-17A remains a dominant pathological effector regardless of cellular source. Energy metabolism of immune cells governs their functional properties¹⁹. The fact that oxalateinduced mitochondrial dysfunction has been described in renal cells and monocytes^{20-22, 24} prompted us to investigate the direct influence of oxalate on Th17 cell differentiation and metabolism. In vitro, we demonstrate that soluble oxalate promotes Th17 differentiation and disrupts mitochondrial function, suggesting that mitochondrial dysfunction may be an upstream modulator of pathogenic T cell polarization under oxalate influence. Pathogenic Th17 have previously been described to rely on increased glycolysis and to a lesser degree on oxidative phosphorylation⁴³. The close connection between loss of mitochondrial function and T cell fate has been described in various pathological, proinflammatory contexts^{44, 45}. In addition, inhibition of mitochondrial respiration triggers ROS production⁴⁶, which in turn is known to induce pathogenic Th17⁴⁷. In line with our transcriptomic analyses of the kidneys confirm dysregulated ROS-related gene expression. In vivo, oxalate-associated

399

400

401

402

403

404

405

406

407

408

409

410

411

412

413

414

415

416

417

418

419

420

421

422

423

424

mitochondrial dysfunction and oxidative stress have been previously linked to inflammation-driven atherosclerosis²³. Together, these findings position oxalate not merely as a crystal-forming irritant but as a direct immunometabolic stressor capable of modulating immune pathways and amplifying inflammation. Consistent with clinical observations linking elevated serum oxalate levels to adverse cardiovascular outcomes and sudden cardiac death in CKD^{6, 7}, our study establishes oxalate as a systemic inflammatory mediator that promotes multiorgan dysfunction via IL-17A. IL-17A is a known promoter of myocardial fibrosis, endothelial dysfunction, and atherosclerosis¹⁸. IL-17A administration in mice induced vascular remodeling and stiffness, resulting in elevated blood pressure⁴⁸. IL-17A overexpression in keratinocytes likewise promoted inflammation, ROS production, and cardiovascular damage ⁴⁹. Clinical data support the relevance of IL-17A after myocardial infarction⁵⁰ and the association of genetic IL-17A and IL-17A receptor variants with CVD mortality⁵¹. IL-17A has been linked to myocardial fibrosis and directed Ly6C^{high} monocytes toward a more proinflammatory phenotype⁵². In line with this, we observe reduced cardiac fibrosis in response to IL-17A blockade. We have previously demonstrated how microbiome-dependent modulation of Th17 affects hypertensive cardiovascular pathologies^{27, 53, 54}. However, our findings do not support a microbiomedependent modulation of Th17 in the context of oxalate. In fact, our microbiome analysis only shows a partial overlap with recently published data from two rat models of oxalate nephropathy, showing among other factors a strong decline in alpha diversity¹³. Such discrepancies could be explained by the use of different experimental diets. Highly standardized, purified diets (as used in our study and in contrast to crude fiber-based chow diets) are known to provide less diverse complex polysaccharides⁵⁵. Consequently, the marked decline in alpha diversity observed in our study following the transition to a purified dietary regime aligns with established concepts wherein dietary fiber serves as a critical substrate for microbial fermentation, sustaining microbial richness and metabolic activity⁵⁶, with no additional effect observed in our study from adding oxalate. More data is needed to disentangle oxalate from experimental diet effects, as well as a detailed reporting of dietary components in experimental studies⁵⁷.

Together, our study challenges the compartmentalized view of oxalate as solely a nephrotoxin and highlight its broader role in the systemic inflammation and cardiovascular comorbidities in oxalate-induced CKD. This work establishes IL-17A as a mediator of oxalate-induced systemic inflammation, with critical implications for understanding sterile injury in crystal-associated nephropathies. The partial therapeutic response to IL-17A blockade underscores the complexity of the innate-adaptive immune interplay and the necessity of targeting interconnected inflammatory pathways. As hyperoxalemia is a conserved risk factor across CKD etiologies^{2, 4, 6}, targeting IL-17A may represent a viable strategy to mitigate CKD-associated inflammation in high-risk populations.

5. Funding

The 4C study was funded by the German Federal Ministry of Education and Research (Project-ID 01EO0802). FACSMelody used in this study was funded by German Federal Ministry of Research, Technology and Space (BMFTR), project-ID: 01EJ2202A. T.S., H.B., and N.W. were supported by the BMFTR, TAhRget consortium (project-ID 01EJ2202A (N.W., H.B.) and 01EJ2202E (T.S.)), as well the QEED consortium (project-ID 13N16386, to H.B.). G.G.S., A.Z. and N.W. were supported by the German Research Foundation (DFG), CRC1470 (project-ID 437531118, subproject A10 to N.W. and A02/ Z01 to G.G.S.), and CRC1525 (project-ID 453989101, to A.Z.) as well as project-ID 432915089 to A.Z. G.G.S. and N.W. were supported from the European Research Council (ERC) under the European Union's Horizon 2020 research and innovation program (852796 to N.W., 101078307 to G.G.S.). NW was supported by the Corona Foundation in the German Stifterverband (S199/10080/2019). G.G.S., R.W. and H.B. were supported by DZHK (German Centre for Cardiovascular Research) project-ID 81X3100227 to R.W., 81X3100210 and 81X2100282 to G.G.S., and 81X3100224 to H.B. R.W was supported by HI-TAC (Helmholtz Institute for Translational AngioCardioScience) Early Career Investigator Grant (7.11442HIEC2401).

6. Author contribution

CRediT: Conceptualization: MIW, MR, FK, NW, HB; Data curation: MIW, HB; Formal Analysis: MIW, MR,

AT, TRL, HB; Funding acquisition: FK, NW, HB; Investigation: MIW, MR, AT, AY, AR, LHG, OP, NG, WA,

SVLC, RW, ON, FS, JH; Methodology: MIW, MR, ON; Project administration: MR, HB; Resources: GGS,

FS, TS, AZ, KUE, FK, NW, HB; Software: MIW, HA, TRL; Supervision: GGS, TS, FK, NW, HB; Validation:

MIW, MR, HA, FK, NW, HB; Visualization: MIW, HB; Writing – original draft: MIW, MR, FK, NW, HB;

Writing – review & editing: all authors.

7. Acknowledgement

We thank Vanessa Riese, Gabriel Kirchgraber, Melanie Röhr and Gudrun Koch for their excellent

technical assistance. We thank the Preclinical Research Center of the MDC for performing plasma BUN

measurements. We thank all regional 4C coordinators for recruiting patients with PH in their respective centers (Sevgi Mir, Betül Sözeri for Izmir (Turkey); Salim Çaliskan, Nur Canpolat and Mahmut Civilibal for Istanbul (Turkey); Yelda Bilginer and Ali Duzova for Ankara centers (Turkey); Aysun K. Bayazit for Adana (Turkey); Bruno Ranchin for Lyon (France)).

8. Conflict of Interest

Conflict of Interest: none declared.

9. References

468

- 469 1. Yang Y, Sharma PD, Nair V, Jhaveri KD, Malieckal DA, Wanchoo R, Rosenstock JL, Bijol V. Kidney
- oxalate crystal deposition in adult patients: A relatively common finding . Clin Nephrol
- 471 2020;**93**:243-250.
- 2. Pfau A, Wytopil M, Chauhan K, Reichel M, Coca SG, Aronson PS, Eckardt KU, Knauf F.
- Assessment of Plasma Oxalate Concentration in Patients With CKD. Kidney Int Rep
- 474 2020;**5**:2013-2020.
- 475 3. Rosenstock JL, Joab TMJ, DeVita MV, Yang Y, Sharma PD, Bijol V. Oxalate nephropathy: a
- 476 review. *Clin Kidney J* 2022;**15**:194-204.
- 477 4. Hawkins-van der Cingel G, Walsh SB, Eckardt KU, Knauf F. Oxalate Metabolism: From Kidney
- 478 Stones to Cardiovascular Disease. *Mayo Clin Proc* 2024;**99**:1149-1161.
- 479 5. Buysschaert B, Aydin S, Morelle J, Gillion V, Jadoul M, Demoulin N. Etiologies, Clinical Features,
- and Outcome of Oxalate Nephropathy. *Kidney Int Rep* 2020;**5**:1503-1509.
- 481 6. Pfau A, Ermer T, Coca SG, Tio MC, Genser B, Reichel M, Finkelstein FO, März W, Wanner C,
- Waikar SS, Eckardt KU, Aronson PS, Drechsler C, Knauf F. High Oxalate Concentrations
- 483 Correlate with Increased Risk for Sudden Cardiac Death in Dialysis Patients. J Am Soc Nephrol
- 484 2021;**32**:2375-2385.
- Nishizawa Y, Miyata S, Tosaka M, Hirasawa E, Hosoda Y, Horimoto A, Omae K, Ito K, Nagano N,
- 486 Hoshino J, Ogawa T. Serum oxalate concentration is associated with coronary artery
- calcification and cardiovascular events in Japanese dialysis patients. *Sci Rep* 2023;**13**:18558.
- 488 8. Mulay SR, Eberhard JN, Pfann V, Marschner JA, Darisipudi MN, Daniel C, Romoli S, Desai J,
- 489 Grigorescu M, Kumar SV, Rathkolb B, Wolf E, Hrabě de Angelis M, Bäuerle T, Dietel B, Wagner
- 490 CA, Amann K, Eckardt KU, Aronson PS, Anders HJ, Knauf F. Oxalate-induced chronic kidney
- disease with its uremic and cardiovascular complications in C57BL/6 mice. Am J Physiol Renal
- 492 *Physiol* 2016;**310**:F785-f795.

493 9. Knauf F, Asplin JR, Granja I, Schmidt IM, Moeckel GW, David RJ, Flavell RA, Aronson PS. NALP3-494 mediated inflammation is a principal cause of progressive renal failure in oxalate nephropathy. 495 Kidney Int 2013;84:895-901. 496 Mulay SR, Kulkarni OP, Rupanagudi KV, Migliorini A, Darisipudi MN, Vilaysane A, Muruve D, Shi 10. 497 Y, Munro F, Liapis H, Anders HJ. Calcium oxalate crystals induce renal inflammation by NLRP3-498 mediated IL-1beta secretion. J Clin Invest 2013;123:236-246. 499 11. Ming S, Tian J, Ma K, Pei C, Li L, Wang Z, Fang Z, Liu M, Dong H, Li W, Zeng J, Peng Y, Gao X. 500 Oxalate-induced apoptosis through ERS-ROS-NF-kappaB signalling pathway in renal tubular 501 epithelial cell. Mol Med 2022;28:88. 502 Holle J, Bartolomaeus H, Lober U, Behrens F, Bartolomaeus TUP, Anandakumar H, Wimmer MI, 12. 503 Vu DL, Kuhring M, Bruning U, Maifeld A, Geisberger S, Kempa S, Schumacher F, Kleuser B, 504 Bufler P, Querfeld U, Kitschke S, Engler D, Kuhrt LD, Drechsel O, Eckardt KU, Forslund SK, 505 Thurmer A, McParland V, Kirwan JA, Wilck N, Muller D. Inflammation in Children with CKD 506 Linked to Gut Dysbiosis and Metabolite Imbalance. J Am Soc Nephrol 2022;33:2259-2275. 507 13. An L, Li S, Chang Z, Lei M, He Z, Xu P, Zhang S, Jiang Z, Iqbal MS, Sun X, Liu H, Duan X, Wu W. 508 Gut microbiota modulation via fecal microbiota transplantation mitigates hyperoxaluria and 509 calcium oxalate crystal depositions induced by high oxalate diet. Gut Microbes 510 2025;**17**:2457490. 511 14. Shee K, Stoller ML. Perspectives in primary hyperoxaluria - historical, current and future clinical 512 interventions. Nat Rev Urol 2022;19:137-146. 513 Kolberg L, Raudvere U, Kuzmin I, Vilo J, Peterson H. gprofiler2 -- an R package for gene list 15. 514 functional enrichment analysis and namespace conversion toolset g:Profiler. F1000Res 2020;9. 515 16. Zhang W, Li L, Zhang T, Gao X, Wang Z, Ming S, Fang Z, Liu M, Dong H, Zhu B, Liao J, Zeng J, 516 Peng Y, Gao X. An Immune Atlas of Nephrolithiasis: Single-Cell Mass Cytometry on SIRT3 517 Knockout and Calcium Oxalate-Induced Renal Injury. J Immunol Res 2021;2021:1260140. 518 17. Querfeld U, Anarat A, Bayazit AK, Bakkaloglu AS, Bilginer Y, Caliskan S, Civilibal M, Doyon A, 519 Duzova A, Kracht D, Litwin M, Melk A, Mir S, Sozeri B, Shroff R, Zeller R, Wuhl E, Schaefer F,

520 Group CS. The Cardiovascular Comorbidity in Children with Chronic Kidney Disease (4C) study: 521 objectives, design, and methodology. Clin J Am Soc Nephrol 2010;5:1642-1648. 522 18. Robert M, Miossec P. Effects of Interleukin 17 on the cardiovascular system. Autoimmun Rev 523 2017;**16**:984-991. 524 19. Hu T, Liu CH, Lei M, Zeng Q, Li L, Tang H, Zhang N. Metabolic regulation of the immune system 525 in health and diseases: mechanisms and interventions. Signal Transduct Target Ther 526 2024;**9**:268. 527 20. Mulay SR, Honarpisheh MM, Foresto-Neto O, Shi C, Desai J, Zhao ZB, Marschner JA, Popper B, 528 Buhl EM, Boor P, Linkermann A, Liapis H, Bilyy R, Herrmann M, Romagnani P, Belevich I, Jokitalo 529 E, Becker JU, Anders HJ. Mitochondria Permeability Transition versus Necroptosis in Oxalate-530 Induced AKI. J Am Soc Nephrol 2019;30:1857-1869. 531 21. Huang MY, Chaturvedi LS, Koul S, Koul HK. Oxalate stimulates IL-6 production in HK-2 cells, a 532 line of human renal proximal tubular epithelial cells. Kidney Int 2005;68:497-503. 533 22. Cao LC, Honeyman TW, Cooney R, Kennington L, Scheid CR, Jonassen JA. Mitochondrial 534 dysfunction is a primary event in renal cell oxalate toxicity. Kidney Int 2004;66:1890-1900. 535 23. Liu Y, Zhao Y, Shukha Y, Lu H, Wang L, Liu Z, Liu C, Zhao Y, Wang H, Zhao G, Liang W, Fan Y, 536 Chang L, Yurdagul A, Jr., Pattillo CB, Orr AW, Aviram M, Wen B, Garcia-Barrio MT, Zhang J, Liu 537 W, Sun D, Hayek T, Chen YE, Rom O. Dysregulated oxalate metabolism is a driver and 538 therapeutic target in atherosclerosis. Cell Rep 2021;36:109420. 539 24. Patel M, Yarlagadda V, Adedoyin O, Saini V, Assimos DG, Holmes RP, Mitchell T. Oxalate 540 induces mitochondrial dysfunction and disrupts redox homeostasis in a human monocyte 541 derived cell line. Redox Biol 2018;15:207-215. 542 25. Kolls JK, Linden A. Interleukin-17 family members and inflammation. Immunity 2004;21:467-543 476. 544 26. Yang J, Zhang L, Yu C, Yang X-F, Wang H. Monocyte and macrophage differentiation: circulation 545 inflammatory monocyte as biomarker for inflammatory diseases. Biomarker Research 546 2014;**2**:1.

547	27.	Bartolomaeus H, Balogh A, Yakoub M, Homann S, Marko L, Hoges S, Tsvetkov D, Krannich A,
548		Wundersitz S, Avery EG, Haase N, Kraker K, Hering L, Maase M, Kusche-Vihrog K, Grandoch M,
549		Fielitz J, Kempa S, Gollasch M, Zhumadilov Z, Kozhakhmetov S, Kushugulova A, Eckardt KU,
550		Dechend R, Rump LC, Forslund SK, Muller DN, Stegbauer J, Wilck N. Short-Chain Fatty Acid
551		Propionate Protects From Hypertensive Cardiovascular Damage. Circulation 2019;139:1407-
552		1421.
553	28.	Speer T, Dimmeler S, Schunk SJ, Fliser D, Ridker PM. Targeting innate immunity-driven
554		inflammation in CKD and cardiovascular disease. Nature Reviews Nephrology 2022;18:762-
555		778.
556	29.	Griffin GK, Newton G, Tarrio ML, Bu DX, Maganto-Garcia E, Azcutia V, Alcaide P, Grabie N,
557		Luscinskas FW, Croce KJ, Lichtman AH. IL-17 and TNF-alpha sustain neutrophil recruitment
558		during inflammation through synergistic effects on endothelial activation. J Immunol
559		2012; 188 :6287-6299.
560	30.	Ge S, Hertel B, Susnik N, Rong S, Dittrich AM, Schmitt R, Haller H, von Vietinghoff S. Interleukin
561		17 receptor A modulates monocyte subsets and macrophage generation in vivo. PLoS One
562		2014; 9 :e85461.
563	31.	Ryu S, Shin JW, Kwon S, Lee J, Kim YC, Bae YS, Bae YS, Kim DK, Kim YS, Yang SH, Kim HY. Siglec-
564		F-expressing neutrophils are essential for creating a profibrotic microenvironment in renal
565		fibrosis. J Clin Invest 2022; 132 .
566	32.	Riedel JH, Paust HJ, Krohn S, Turner JE, Kluger MA, Steinmetz OM, Krebs CF, Stahl RA, Panzer
567		U. IL-17F Promotes Tissue Injury in Autoimmune Kidney Diseases. J Am Soc Nephrol
568		2016; 27 :3666-3677.
569	33.	Chung Y, Chang SH, Martinez GJ, Yang XO, Nurieva R, Kang HS, Ma L, Watowich SS, Jetten AM,
570		Tian Q, Dong C. Critical regulation of early Th17 cell differentiation by interleukin-1 signaling.
571		Immunity 2009; 30 :576-587.

572 Sun D, Novotny M, Bulek K, Liu C, Li X, Hamilton T. Treatment with IL-17 prolongs the half-life 34. 573 of chemokine CXCL1 mRNA via the adaptor TRAF5 and the splicing-regulatory factor SF2 (ASF). 574 Nat Immunol 2011;12:853-860. 575 El-Behi M, Ciric B, Dai H, Yan Y, Cullimore M, Safavi F, Zhang GX, Dittel BN, Rostami A. The 35. 576 encephalitogenicity of T(H)17 cells is dependent on IL-1- and IL-23-induced production of the 577 cytokine GM-CSF. Nat Immunol 2011;12:568-575. 578 36. Shahrara S, Pickens SR, Mandelin AM, 2nd, Karpus WJ, Huang Q, Kolls JK, Pope RM. IL-17-579 mediated monocyte migration occurs partially through CC chemokine ligand 2/monocyte 580 chemoattractant protein-1 induction. J Immunol 2010;184:4479-4487. 581 Pruenster M, Immler R, Roth J, Kuchler T, Bromberger T, Napoli M, Nussbaumer K, Rohwedder 37. 582 I, Wackerbarth LM, Piantoni C, Hennis K, Fink D, Kallabis S, Schroll T, Masgrau-Alsina S, Budke 583 A, Liu W, Vestweber D, Wahl-Schott C, Roth J, Meissner F, Moser M, Vogl T, Hornung V, Broz 584 P, Sperandio M. E-selectin-mediated rapid NLRP3 inflammasome activation regulates 585 S100A8/S100A9 release from neutrophils via transient gasdermin D pore formation. Nat 586 Immunol 2023;24:2021-2031. 587 38. Ermer T, Nazzal L, Tio MC, Waikar S, Aronson PS, Knauf F. Oxalate homeostasis. Nat Rev 588 Nephrol 2023;19:123-138. 589 39. Yang BH, Hagemann S, Mamareli P, Lauer U, Hoffmann U, Beckstette M, Fohse L, Prinz I, 590 Pezoldt J, Suerbaum S, Sparwasser T, Hamann A, Floess S, Huehn J, Lochner M. Foxp3(+) T cells 591 expressing RORgammat represent a stable regulatory T-cell effector lineage with enhanced 592 suppressive capacity during intestinal inflammation. Mucosal Immunol 2016;9:444-457. 593 40. Beriou G, Costantino CM, Ashley CW, Yang L, Kuchroo VK, Baecher-Allan C, Hafler DA. IL-17-594 producing human peripheral regulatory T cells retain suppressive function. Blood 595 2009;**113**:4240-4249. 596 41. Holzer MT, Almanzar G, Woidich R, Hugle B, Haas JP, Prelog M. Mitigated suppressive function 597 of regulatory T cells (Treg) upon Th17-inducing cytokines in oligo- and polyarticular Juvenile 598 Idiopathic Arthritis (JIA) patients. Pediatr Rheumatol Online J 2022;20:26.

600

601

602

603

604

605

606

607

608

609

610

611

612

613

614

615

616

617

618

619

620

621

622

623

624

42. Zhu C, Liang Q, Liu Y, Kong D, Zhang J, Wang H, Wang K, Guo Z. Kidney injury in response to crystallization of calcium oxalate leads to rearrangement of the intrarenal T cell receptor delta immune repertoire. J Transl Med 2019;17:278. Wu L, Hollinshead KER, Hao Y, Au C, Kroehling L, Ng C, Lin WY, Li D, Silva HM, Shin J, Lafaille JJ, 43. Possemato R, Pacold ME, Papagiannakopoulos T, Kimmelman AC, Satija R, Littman DR. Niche-Selective Inhibition of Pathogenic Th17 Cells by Targeting Metabolic Redundancy. Cell 2020;182:641-654 e620. 44. Desdin-Mico G, Soto-Heredero G, Aranda JF, Oller J, Carrasco E, Gabande-Rodriguez E, Blanco EM, Alfranca A, Cusso L, Desco M, Ibanez B, Gortazar AR, Fernandez-Marcos P, Navarro MN, Hernaez B, Alcami A, Baixauli F, Mittelbrunn M. T cells with dysfunctional mitochondria induce multimorbidity and premature senescence. Science 2020;368:1371-1376. 45. Scharping NE, Rivadeneira DB, Menk AV, Vignali PDA, Ford BR, Rittenhouse NL, Peralta R, Wang Y, Wang Y, DePeaux K, Poholek AC, Delgoffe GM. Mitochondrial stress induced by continuous stimulation under hypoxia rapidly drives T cell exhaustion. Nat Immunol 2021;22:205-215. 46. Li N, Ragheb K, Lawler G, Sturgis J, Rajwa B, Melendez JA, Robinson JP. Mitochondrial complex I inhibitor rotenone induces apoptosis through enhancing mitochondrial reactive oxygen species production. J Biol Chem 2003;278:8516-8525. 47. Bonetti L, Horkova V, Grusdat M, Longworth J, Guerra L, Kurniawan H, Franchina DG, Soriano-Baguet L, Binsfeld C, Verschueren C, Spath S, Ewen A, Koncina E, Gerardy JJ, Kobayashi T, Dostert C, Farinelle S, Harm J, Fan YT, Chen Y, Harris IS, Lang PA, Vasiliou V, Waisman A, Letellier E, Becher B, Mittelbronn M, Brenner D. A Th17 cell-intrinsic glutathione/mitochondrial-IL-22 axis protects against intestinal inflammation. Cell Metab 2024;36:1726-1744 e1710. 48. Orejudo M, Garcia-Redondo AB, Rodrigues-Diez RR, Rodrigues-Diez R, Santos-Sanchez L, Tejera-Munoz A, Egido J, Selgas R, Salaices M, Briones AM, Ruiz-Ortega M. Interleukin-17A induces vascular remodeling of small arteries and blood pressure elevation. Clin Sci (Lond) 2020;**134**:513-527.

625 Karbach S, Croxford AL, Oelze M, Schuler R, Minwegen D, Wegner J, Koukes L, Yogev N, 49. 626 Nikolaev A, Reissig S, Ullmann A, Knorr M, Waldner M, Neurath MF, Li H, Wu Z, Brochhausen 627 C, Scheller J, Rose-John S, Piotrowski C, Bechmann I, Radsak M, Wild P, Daiber A, von Stebut E, 628 Wenzel P, Waisman A, Munzel T. Interleukin 17 drives vascular inflammation, endothelial 629 dysfunction, and arterial hypertension in psoriasis-like skin disease. Arterioscler Thromb Vasc 630 Biol 2014;34:2658-2668. 631 50. Bochaton T, Mewton N, Thiam N, Lavocat F, Baetz D, Dufay N, Prieur C, Bonnefoy-Cudraz E, 632 Miossec P, Ovize M. Early kinetics of serum Interleukine-17A and infarct size in patients with 633 reperfused acute ST-elevated myocardial infarction. PLoS One 2017;12:e0188202. 634 51. Sandip C, Tan L, Huang J, Li Q, Ni L, Cianflone K, Wang DW. Common variants in IL-17A/IL-17RA 635 axis contribute to predisposition to and progression of congestive heart failure. Medicine 636 (Baltimore) 2016;95:e4105. 637 52. Wu L, Ong S, Talor MV, Barin JG, Baldeviano GC, Kass DA, Bedja D, Zhang H, Sheikh A, Margolick 638 JB, Iwakura Y, Rose NR, Cihakova D. Cardiac fibroblasts mediate IL-17A-driven inflammatory 639 dilated cardiomyopathy. J Exp Med 2014;211:1449-1464. 640 53. Avery EG, Bartolomaeus H, Rauch A, Chen CY, N'Diaye G, Lober U, Bartolomaeus TUP, Fritsche-641 Guenther R, Rodrigues AF, Yarritu A, Zhong C, Fei L, Tsvetkov D, Todiras M, Park JK, Marko L, 642 Maifeld A, Patzak A, Bader M, Kempa S, Kirwan JA, Forslund SK, Muller DN, Wilck N. 643 Quantifying the impact of gut microbiota on inflammation and hypertensive organ damage. 644 Cardiovasc Res 2023;119:1441-1452. 645 54. Wilck N, Matus MG, Kearney SM, Olesen SW, Forslund K, Bartolomaeus H, Haase S, Mahler A, 646 Balogh A, Marko L, Vvedenskaya O, Kleiner FH, Tsvetkov D, Klug L, Costea PI, Sunagawa S, 647 Maier L, Rakova N, Schatz V, Neubert P, Fratzer C, Krannich A, Gollasch M, Grohme DA, Corte-648 Real BF, Gerlach RG, Basic M, Typas A, Wu C, Titze JM, Jantsch J, Boschmann M, Dechend R, 649 Kleinewietfeld M, Kempa S, Bork P, Linker RA, Alm EJ, Muller DN. Salt-responsive gut 650 commensal modulates TH17 axis and disease. Nature 2017;551:585-589.

651 55. Pellizzon M. Choice of laboratory animal diet influences intestinal health. Lab Anim (NY) 652 2016;**45**:238-239. 653 56. Sonnenburg JL, Sonnenburg ED. Vulnerability of the industrialized microbiota. Science 654 2019;366. 655 Klurfeld DM, Davis CD, Karp RW, Allen-Vercoe E, Chang EB, Chassaing B, Fahey GC, Jr., Hamaker 57. 656 BR, Holscher HD, Lampe JW, Marette A, Martens E, O'Keefe SJ, Rose DJ, Saarela M, Schneeman 657 BO, Slavin JL, Sonnenburg JL, Swanson KS, Wu GD, Lynch CJ. Considerations for best practices 658 in studies of fiber or other dietary components and the intestinal microbiome. Am J Physiol 659 Endocrinol Metab 2018;315:E1087-E1097.

Figure Legends

Figure 1. High oxalate diet leads to kidney damage and systemic immune activation. a) C57Bl6/N mice were placed on a high oxalate (Ox, n=7) or control chow diet (Chow, n=7). b) Relative body weight changes, c) blood urea nitrogen (BUN), d) plasma oxalate levels and e) renal mRNA expression of the kidney damage marker Lcn2 at the endpoint. f) Volcano plot of differentially expressed genes from bulk mRNA sequencing of kidney tissue (n=3 per group) and g) pathway enrichment analysis. h) Heatmap of renal immune cell populations derived from flow cytometry. i) Principal component analysis (PCA) of immune profiles from spleen, kidney, and intestinal lamina propria lymphocytes (LPL). Absolute quantification of leukocytes counts from the j) spleen and the k) kidney. Mann-Whitney U test was used for all group comparisons, for f, g) false discovery correction according to Benjamini-Hochberg was performed. Box plots display the median and interquartile range (IQR, 25th–75th percentile); whiskers extend to the most extreme values within 1.5x IQR. Each dot represents a single mouse.

Figure 2. RORyt expressing T cells expand in multiple organs during high oxalate diet. a) Principal component analyses (PCA) of immune cells isolated from the kidney, the lamina propria of the small intestine (siLPL) and the large intestine (cLPL). b) The 15 highest loading (immune cell populations) of the PC that separate oxlate diet (Ox)-fed mice (n=7) from control chow diet (Chow)-fed mice (n=7) for each organ. c) Venn diagram of these 15 immune cell populations. d) Boxplots of the two overlapping immune cell populations: RORyt+ conventional T helper cells (Tconv, CD45+ CD3+ gdTCR- CD4+ CD8-FoxP3-) and RORyt+ regulatory T cells (Treg, CD45+ CD3+ gdTCR- CD4+ CD8-FoxP3-). e) Representative plots for RORgt (and Tbet) gated out of Tconv and Treg isolated from kidney. f) RORyt+ Tconv and g) RORyt+ Treg in the spleen. h) Upregulated T cell pathways from kidney bulk mRNA sequencing (n=3 per group). i) Heatmap of genes belonging to the KEGG IL-17A signaling pathway. Mann-Whitney U test was used for all group comparisons, for h) false discovery correction according to Benjamini-Hochberg was performed. j) IL-17A plasma levels in primary hyperoxaluria (PH, n=8) patients and healthy controls (n=20), p-value from two-tailed Student's t-test. Box plots display the median and interquartile range

688

689

690

691

692

693

694

695

696

697

698

699

700

701

702

703

704

705

706

707

708

709

710

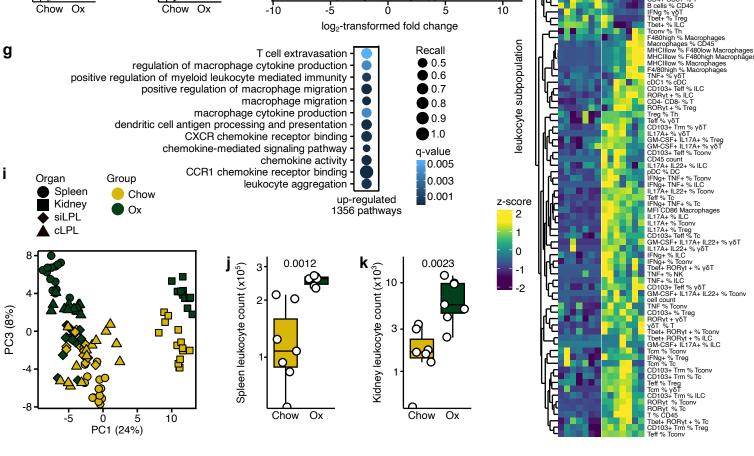
711

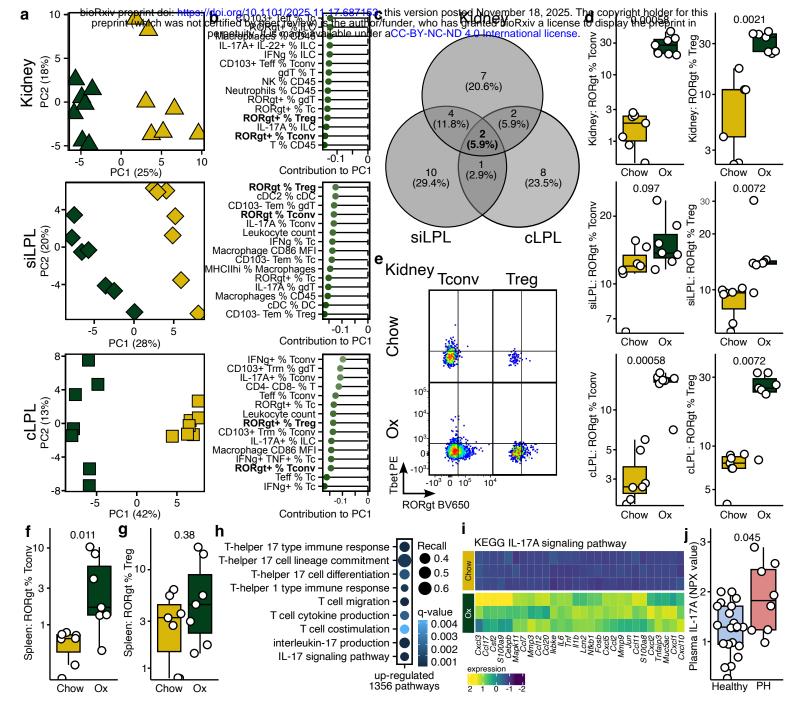
712

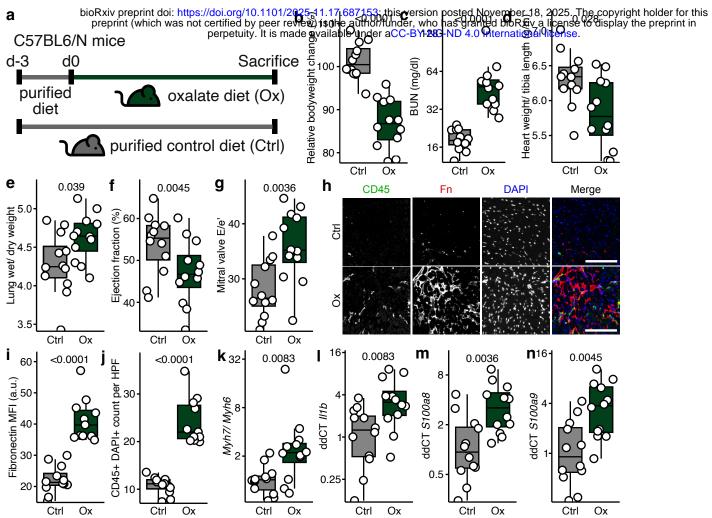
713

(IQR, 25th-75th percentile); whiskers extend to the most extreme values within 1.5x IQR. Each dot represents a single mouse. For PCA, each dot represents one individual. Figure 3. High oxalate diet induces cardiac damage and impairs cardiac function. a) C57BI6/N mice placed on an oxalate diet (Ox, n=12) or purified control diet (Ctrl, n=12). b) Relative body weight change, c) blood urea nitrogen (BUN), d) normalised heart weight and e) lung wet/ dry weight at the endpoint. f) Echocardiographic analysis of the ejection fraction and g) mitral valve E/e'. h) Representative histological pictures (scale bar = 100μm), analysis of i) cardiac fibrosis (Fibronectin MFI) and i) cardiac immune cell infiltration. k) Cardiac gene expression analysis of Mhy7/Mhy6 ratio, l) II1b, m) S100a8 and n) S100a9.. Mann-Whitney U test (two-tailed) was used for all group comparisons. Box plots display the median and interquartile range (IQR, 25th-75th percentile); whiskers extend to the most extreme values within 1.5x IQR. Each dot represents a single mouse. Figure 4. Oxalate in vitro aggravates Th17 differentiation and inhibits the mitochondrial function. a) Naïve T cells (CD4+ CD25- CD44- CD62L+) were isolated from C57BL6 mice. Naïve T cells were differentiated into Th17 cells in the presence of different concentrations of soluble oxalate (sodium oxalate, NaOx) and their mitochondrial function was assessed by real-time extracellular flux analysis. b) Representative zebra plots of IL-17A expression and boxplot of normalized Th17 differentiation. c) Oxygen consumption rate (OCR) during mitochondrial stress test assay by Seahorse (Agilent). d) Boxplot of basal respiration rate, e) ATP-linked respiration rate, f) maximal respiration capacity and g) spare respiratory capacity. The values are shown as raw data with each dot representing the data from technical replicates from 2-3 independent experiments. Student's T test (two-tailed) was used for group comparisons. Box plots display the median and interquartile range (IQR, 25th-75th percentile); whiskers extend to maximum and minimum values. Figure 5. Antibody-mediated IL-17A neutralization reduces cardiorenal damage by high oxalate diet. C57Bl6/N mice placed on a high oxalate were thrice weekly injected with an IL-17A-neutralizing

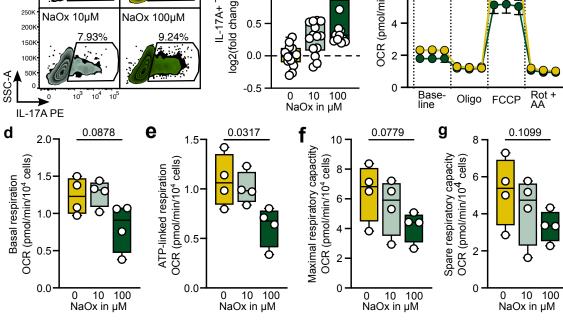
antibody (n=12) or IgG control (n=12). a) Longitudinal relative body weight bodyweight changes (dots represent mean, error bars indicate standard deviation) and b) relative body weight change at the endpoint. c) Blood urea nitrogen (BUN) at endpoint. d) Sirius red staining of kidney tissue (right, scale bar = 200μm) with identification of fibrosis signal (left, scale bar = 200μm) and e) quantification of kidney fibrosis. renal mRNA expression of the kidney damage marker f) *Lcn2* and key inflammation markers g) *ll1b* and h) *Tnf* at the endpoint. i) Kidney leukocytes infiltration, j) splenic neutrophil share, and k) kidney neutrophil. l) Normalised heart weight and m) lung wet / dry weight at the endpoint. n) Histological analysis (scale bar = 100μm) of o) cardiac fibrosis (Fibronectin MFI) and p) cardiac immune cell infiltration. q) Cardiac gene expression analysis of *Mhy7/Mhy6* and r) *S100a8*. One-sided Mann-Whitney U test was used for all group comparisons. Box plots display the median and interquartile range (IQR, 25th–75th percentile); whiskers extend to the most extreme values within 1.5x IQR. Each dot represents a single mouse.







а



IgG αIL17A

Ох

IgG αIL17A

Ох

lgG

Ох

αIL17A

Ох